Local order controls the onset of oscillations in the nonreciprocal Ising model

Kristian Blom [1], Uwe Thiele [2,3,4] and Aljaž Godec [1,*]

[1] *Mathematical bioPhysics group, Max Planck Institute for Multidisciplinary Sciences, 37077 Göttingen, Germany*

[2] *Institute of Theoretical Physics, University of Münster, 48149 Münster, Germany*

[3] *Center for Nonlinear Science (CeNoS), University of Münster, 48149 Münster, Germany*

[4] *Center for Multiscale Theory and Computation (CMTC), University of Münster, 48149 Münster, Germany*

(Received 29 July 2024; accepted 17 January 2025; published 12 February 2025)

We elucidate the generic bifurcation behavior of local and global order in the nonreciprocal Ising model evolving under Glauber dynamics. We show that a critical magnitude of nearest-neighbor correlations within the respective lattices controls the emergence of coherent oscillations of global order as a result of frustration. Local order is maintained during these oscillations, implying nontrivial spatiotemporal correlations. Long-lived states emerge in the strong-interaction regime. The residence time in either of these states eventually diverges, giving rise to ordered nonequilibrium trapped states and a loss of ergodic behavior via a saddle-node-infinite-period bifurcation. Our work provides a comprehensive microscopic understanding of the nonreciprocal Ising model beyond the mean-field approximation.

DOI: 10.1103/PhysRevE.111.024207

I. INTRODUCTION

The last decade saw a surge of interest in many-body lattice systems with nonreciprocal interactions [1–11]. At the microscopic level, nonreciprocal interactions violate Newton's third law and result in broken detailed balance [12,13], thereby driving the system out of equilibrium. On the collective level, nonreciprocally interacting systems can resist coarsening and self-organize into dynamic states with unique spatiotemporal patterns, including traveling and oscillatory states [14–22]. Phenomenologically, such systems are typically described using nonvariational couplings of Allen-Cahn models (for nonconserved dynamics) or Cahn-Hilliard models (for conserved dynamics), corresponding to models A and B, respectively, as outlined in [23].

By introducing two nonreciprocally coupled Ising lattices, various studies have shown under which conditions nonreciprocity induces temporal oscillations in the magnetization [1–7]. These works revealed intriguing phenomena, such as Hopf instabilities [1,2,6,7], saddle-node bifurcations [7,24], and hidden collective oscillations [2]. However, so far these studies have been limited to phenomenological and mean-field theory, raising the question to what extent these results apply beyond their respective approximations.

Here, we go beyond mean-field reasoning and explicitly incorporate nearest-neighbor correlations into a thermodynamically consistent description of two nonreciprocally coupled Ising models. We consider both *global and local order*, and explain why a critical magnitude of nearest-neighbor correlations controls the symmetry-breaking transition in the global order, in turn bounding the onset of coherent oscillations. We elucidate how the bifurcation behavior depends on the interaction strength and highlight stark differences in the spatiotemporal dynamics of all-to-all (mean-field) versus short-range-interacting systems; the square and Bethe lattices display equivalent behavior that is strikingly different from the all-to-all lattice.

II. MODEL

Consider a pair of lattices denoted by $\mu = a, b$, as shown in Fig. 1(a), each having a coordination number z and periodic boundary conditions. On each lattice there are N spins that can assume two states $\sigma_i^\mu = \pm 1$, with $i \in \{1, ..., N\}$ enumerating the spin's location. Each spin interacts with its z nearest neighbors on the same lattice and the spin at the equivalent position on the opposing lattice. The *local* interaction energy [25] of spin i on lattice μ can be written as

$$E_i^\mu = -J_\mu \sigma_i^\mu \sum_{\langle i|j \rangle} \sigma_j^\mu - K_\mu \sigma_i^a \sigma_i^b, \tag{1}$$

where $\langle i|j \rangle$ denotes a sum over nearest neighbors j of spin i. Throughout, we express energies in units of $k_B T$, where T is the temperature of the heat bath. The parameter J_μ denotes the coupling within lattice μ, and K_μ denotes the (directed) coupling between the spins in μ and those of the opposing lattice, respectively. When $K_a \neq K_b$, equivalent spins on the opposing lattices interact nonreciprocally.

We consider single spin-flip Glauber dynamics [26]. Let $P(\boldsymbol{\sigma}; t)$ be the probability at time t to find the system in state $\boldsymbol{\sigma} = \{\sigma_1^a, \sigma_1^b, ..., \sigma_N^a, \sigma_N^b\}$, which is governed by the master

*Contact author: agodec@mpinat.mpg.de

equation

$$\frac{\mathrm{d}P(\boldsymbol{\sigma};t)}{\mathrm{d}t} = \sum_{\mu,i} w_i^{\mu}\big(-\sigma_i^{\mu}\big)P(\boldsymbol{\sigma}'_{\mu,i};t) - w_i^{\mu}\big(\sigma_i^{\mu}\big)P(\boldsymbol{\sigma};t), \quad (2)$$

where $\boldsymbol{\sigma}'_{\mu,i} = \{\sigma_1^a, \sigma_1^b, ..., -\sigma_i^{\mu}, ..., \sigma_N^a, \sigma_N^b\}$ is a state which differs from state $\boldsymbol{\sigma}$ by one spin flip. The transition rates $w_i^{\mu}(\sigma_i^{\mu})$ to flip a spin $\sigma_i^{\mu} \to -\sigma_i^{\mu}$ are uniquely specified by limiting the interactions to nearest neighbors, imposing isotropy in position space, and requiring that for $K_a = K_b$ the transition rates obey detailed balance. These physical restrictions then lead to the general result [1,2]

$$w_i^{\mu}\big(\sigma_i^{\mu}\big) = \big[1 - \tanh\big(\Delta E_i^{\mu}/2\big)\big]/2\tau, \quad (3)$$

where $\Delta E_i^{\mu} = -2E_i^{\mu}$ is the change in energy on the $\mu = a, b$ lattice after spin conversion $\sigma_i^{\mu} \to -\sigma_i^{\mu}$, and τ is an intrinsic timescale to attempt a single spin flip.

A. Global and local order parameters

We are interested in the temporal dynamics of global and local order parameters averaged over all spins. The magnetization or global order is given by [27]

$$m^{\mu}(t) \equiv \frac{1}{N}\sum_{i=1}^{N}\big\langle\sigma_i^{\mu}(t)\big\rangle \in [-1, 1], \quad (4)$$

where $\langle f(t)\rangle \equiv \sum_{\boldsymbol{\sigma}} P(\boldsymbol{\sigma};t)f(\boldsymbol{\sigma})$. The three local order parameters are [27]

$$q^{\mu\mu}(t) \equiv \frac{1}{zN}\sum_{i=1}^{N}\sum_{\langle i|j\rangle}\big\langle\sigma_i^{\mu}(t)\sigma_j^{\mu}(t)\big\rangle \in [-1, 1], \quad (5)$$

$$q^{ab}(t) \equiv \frac{1}{N}\sum_{i=1}^{N}\big\langle\sigma_i^{a}(t)\sigma_i^{b}(t)\big\rangle \in [-1, 1], \quad (6)$$

with correlations

$$\mathcal{C}^{\mu\nu}(t) \equiv q^{\mu\nu}(t) - m^{\mu}(t)m^{\nu}(t). \quad (7)$$

We distinguish between the local order within and between the lattices. The alignment of spin pairs within lattice μ is quantified by $q^{\mu\mu}(t)$, and $q^{ab}(t)$ (also known as the overlap [28,29]) measures the alignment of equivalent spins between both lattices. The normalization in Eq. (5) arises because zN is the number of nearest-neighbor pairs (including double counting) in a periodic lattice with coordination number z.

B. Evolution equations beyond the mean-field approximation

Our first main result is an *exact* set of coupled differential equations for the order parameters in the thermodynamic limit $N \to \infty$, which reads (see Appendix A for a detailed derivation)

$$\tau\frac{\mathrm{d}m^{\mu}(t)}{\mathrm{d}t} + m^{\mu}(t) = \sum_{l,n}\mathcal{P}_{l,n}^{\mu}(t)\tanh\big(U_{l,n}^{\mu}\big), \quad (8)$$

$$\tau\frac{\mathrm{d}q^{\mu\mu}(t)}{\mathrm{d}t} + 2q^{\mu\mu}(t) = \frac{2}{z}\sum_{l,n}(2l - z)\mathcal{P}_{l,n}^{\mu}(t)\tanh\big(U_{l,n}^{\mu}\big), \quad (9)$$

$$\tau\frac{\mathrm{d}q^{ab}(t)}{\mathrm{d}t} + 2q^{ab}(t) = \sum_{\mu}\sum_{l,n}(2n - 1)\mathcal{P}_{l,n}^{\mu}(t)\tanh\big(U_{l,n}^{\mu}\big), \quad (10)$$

where $\sum_{l,n} \equiv \sum_{l=0}^{z}\sum_{n=0}^{1}$ is a sum over all possible values of neighboring up spins on the same ($l \in \{0, \ldots, z\}$) and opposing ($n \in \{0, 1\}$) lattice, and

$$U_{l,n}^{\mu} \equiv [2l - z]J_{\mu} + [2n - 1]K_{\mu} \quad (11)$$

parametrizes the change in energy upon flipping a spin with such a local environment. Finally, $\mathcal{P}_{l,n}^{\mu}(t) \in [0, 1]$ is the time-dependent probability of selecting an up or down spin that has l neighboring up spins on the same lattice and n neighboring up spins on the opposing lattice. The probability is normalized as

$$\sum_{l,n}\mathcal{P}_{l,n}^{\mu}(t) = 1. \quad (12)$$

Equations (8)–(10) are not yet closed; evaluating $\mathcal{P}_{l,n}^{\mu}(t)$ for an arbitrary lattice is a daunting combinatorial task, as it depends on microscopic details and, therefore, on an infinite hierarchy of order parameters. However, we can approximate $\mathcal{P}_{l,n}^{\mu}(t)$ to different levels of accuracy, which we do in the next section.

Note that evolution equations for the nonreciprocal Ising model on the fully connected mean-field lattice have been constructed in [7], and are reported in Appendix E for completeness.

C. Bethe-Guggenheim approximation

An accurate closed-form expression for $\mathcal{P}_{l,n}^{\mu}(t)$ can be obtained with the Bethe-Guggenheim (BG) approximation (or pair approximation), where we assume perfect mixing of nearest-neighbor spin pairs. This approximation is exact on loopless lattices such as the Bethe lattice [30], or large random graphs with fixed coordination number [31,32]. As we show in Sec. V, the spatiotemporal dynamics on these lattices agree qualitatively with the behavior on the square lattice, in contrast to that on the mean-field lattice. We split $\mathcal{P}_{l,n}^{\mu}(t)$ in "up" and "down" spin contributions

$$\mathcal{P}_{l,n}^{\mu}(t) = \mathcal{P}_{l,n}^{\mu+}(t) + \mathcal{P}_{l,n}^{\mu-}(t), \quad (13)$$

where, e.g., $\mathcal{P}_{l,n}^{\mu+}(t) \in [0, 1]$ is the probability of flipping an up spin with l up neighbors on the same lattice and n up neighbors on the opposing lattice, respectively. These probabilities are derived in Appendix B and read (omitting the explicit t dependence on the right-hand side)

$$\mathcal{P}_{l,n}^{a\pm}(t) = \frac{C_l^z(1\pm 2m^a + q^{aa})^{\delta_l^{\pm}}(1\pm m^a - m^b \mp q^{ab})^{1-n}}{(1\pm m^a)^z(1-q^{aa})^{-\delta_l^{\mp}}(1\pm m^a + m^b \pm q^{ab})^{-n}}, \quad (14)$$

where $\delta_l^{+} = l$, $\delta_l^{-} = z - l$, and

$$C_l^z \equiv \frac{1}{2^{z+2}}\binom{z}{l}. \quad (15)$$

The expression for $\mathcal{P}_{l,n}^{b\pm}(t)$ follows from Eq. (14) by interchanging $m^a \leftrightarrow m^b$ and $q^{aa} \leftrightarrow q^{bb}$. Inserting Eq. (14) into Eqs. (8)–(10) yields a closed system of five coupled nonlinear differential equations.

III. LINEAR ANALYSIS AND THE HOPF BIFURCATION

We focus on the symmetric nonreciprocal setting $J_a = J_b = J$ and $K_a = -K_b = K$, also known as the perfectly non-

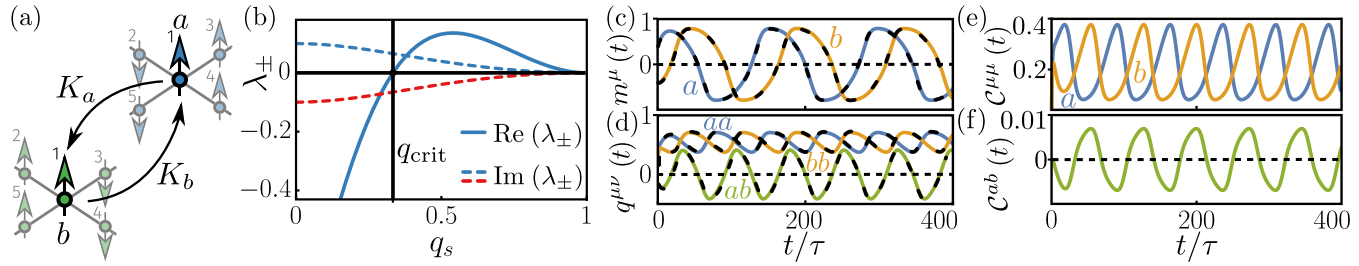

FIG. 1. (a) Schematic of two Ising lattices a and b with coordination number $z = 4$ and cross-coupling (K_a, K_b). For $K_a \neq K_b$ the cross-coupling is nonreciprocal. (b) Eigenvalues $\lambda_\pm$ of the linear stability matrix [Eq. (22)] as a function of the steady-state local order q_s for $K_a = -K_b = 0.1$. When $q_s \geqslant q_{\rm crit}$ [black vertical line; Eq. (20)] the real parts of $\lambda_\pm$ are non-negative, resulting in coherent oscillations. (c)–(f) Temporal evolution of the magnetization $m^\mu(t)$ [Eq. (4)], local order $q^{\mu\nu}(t)$ [Eqs. (5) and (6)], and local correlations $\mathcal{C}^{\mu\nu}(t)$ [Eq. (7)] for $K_a = -K_b = K = 0.1$ and $J_a = J_b = 0.4$. Black dashed lines in (c) and (d) are obtained with Monte Carlo simulations on the Bethe lattice (see Appendix G for details). In all panels we consider $z = 4$.

reciprocal setting [33], while keeping z general. We start with the linear stability analysis of the steady states of Eqs. (8)–(10). The trivial steady state is given by $m_s^\mu = 0$, $q_s^{ab} = 0$, and

$$q_s^{\mu\mu} \equiv q_s(J, K), \tag{16}$$

which is explicitly given in Appendix C for various values of z. To first order, small perturbations $\delta\mathbf{m}(t) \equiv [\delta m^a(t), \delta m^b(t)]$ decouple from perturbations $\delta\mathbf{q}(t) \equiv [\delta q^{aa}(t), \delta q^{bb}(t), \delta q^{ab}(t)]$, and we obtain the linear equation

$$\tau \frac{\mathrm{d}\delta\mathbf{m}(t)}{\mathrm{d}t} = \begin{pmatrix} M_1(q_s;J,K) & -M_2(q_s;J,K) \\ M_2(q_s;J,K) & M_1(q_s;J,K) \end{pmatrix} \delta\mathbf{m}(t). \tag{17}$$

The linear equation for $\delta\mathbf{q}(t)$ is given in [34] and does not play any further role here. The elements of the linear stability matrix read

$$M_1(q_s;J,K) = \frac{q_s/q_{\rm crit} - 1}{1 + q_s}\left[1 - 2\sum_{l,n} \overline{\mathcal{P}}_l^+ \tanh\left(U_{l,n}^a\right)\right],$$
$$M_2(q_s;J,K) = \sum_{l,n}(2n-1)[\overline{\mathcal{P}}_l^+ + \overline{\mathcal{P}}_l^-]\tanh\left(U_{l,n}^a\right), \tag{18}$$

where

$$\overline{\mathcal{P}}_l^\pm(q_s) \equiv \mathcal{C}_l^z(1 \mp q_s)^{z-l}(1 \pm q_s)^l \tag{19}$$

are the probabilities (14) evaluated at steady-state values, and we introduced the critical local order

$$q_{\rm crit} \equiv \frac{1}{z-1}, \tag{20}$$

which *only* depends on the coordination number of the lattice, and sets a critical value for the steady-state local order. The solution of the linear stability equation can be written as

$$\delta\mathbf{m}(t) = \sum_{k=\pm} \mathcal{A}_k \mathrm{e}^{\lambda_k t/\tau} \boldsymbol{v}_k, \tag{21}$$

where $\mathcal{A}_\pm$ are set by the initial conditions, $\boldsymbol{v}_\pm = (\mp\mathrm{i}, 1)^{\mathrm{T}}$ are the eigenvectors of the linear stability matrix, and the corresponding eigenvalues are

$$\lambda_\pm(q_s;J,K) = M_1(q_s;J,K) \pm \mathrm{i}M_2(q_s;J,K), \tag{22}$$

i being the imaginary unit. Since $M_2(q_s;J,K \neq 0) \neq 0$ (see proof in Appendix D), the eigenvalues are complex for $K \neq 0$ [see dashed lines in Fig. 1(b)], resulting in oscillatory perturbations. The Hopf bifurcation [35], also called type-$\mathrm{II_o}$ instability [36], occurs when complex conjugate eigenvalues transit the imaginary axis in the complex plane. According to Eq. (22) this occurs when $M_1(q_s;J,K) = 0$ implying $q_s(J,K) = q_{\rm crit}$ as seen from Eq. (18). The Hopf bifurcation is thus set by the critical value $q_{\rm crit}$ for local order, and for $q_s > q_{\rm crit}$ we have $\mathrm{Re}(\lambda_\pm) > 0$ [solid line in Fig. 1(b)]. In other words, when spins on the respective lattices are sufficiently aligned, a transition to an oscillatory state occurs as shown in Figs. 1(c) and 1(d).

The critical value of the local order that determines the onset of coherent oscillations is our second main result that generalizes to other approximation schemes beyond the mean-field approximation (see Appendix F). After sufficient local order is attained within the lattices, the frustration due to the nonreciprocal coupling gives rise to coherent oscillations: for $K > 0$ a spin σ_i^a wants to align with σ_i^b that, in turn, tends to misalign with σ_i^a. This dynamic frustration results in an oscillatory motion of the order parameters [33]. Notably, for the one-dimensional lattice ($z = 2$) we see from Eq. (20) that $q_{\rm crit} = 1$, which, in contrast to the mean-field prediction [7] (see also Appendix E), correctly implies the nonexistence of a Hopf bifurcation.

IV. NONLINEAR ANALYSIS AND THE SNIPER BIFURCATION

Going beyond linear stability, we perform a nonlinear analysis of Eqs. (8)–(10) through numerical continuation [37]. The resulting bifurcation diagrams are shown in Figs. 2(a) and 2(b) and the complete phase diagram in Fig. 2(d), which we now explain in detail.

We start with the noninteracting case with $K = 0$ [see Fig. 2(a)]. For small values of J, there exists only one (trivial) stable steady state with $m_s^\mu = 0$, as explained in the previous section. Increasing J to $\ln[z/(z-2)]/2$ we find a pitchfork bifurcation [red dot in Fig. 2(a)], which coincides with $q_s(J,0) = q_{\rm crit}$, and beyond which the trivial state becomes unstable. At the pitchfork bifurcation, four stable branches [blue lines in Fig. 2(a)] and four unstable branches [red dashed lines in Fig. 2(a)] of steady states emerge. Unstable branches have zero magnetization in one of the lattices, while stable

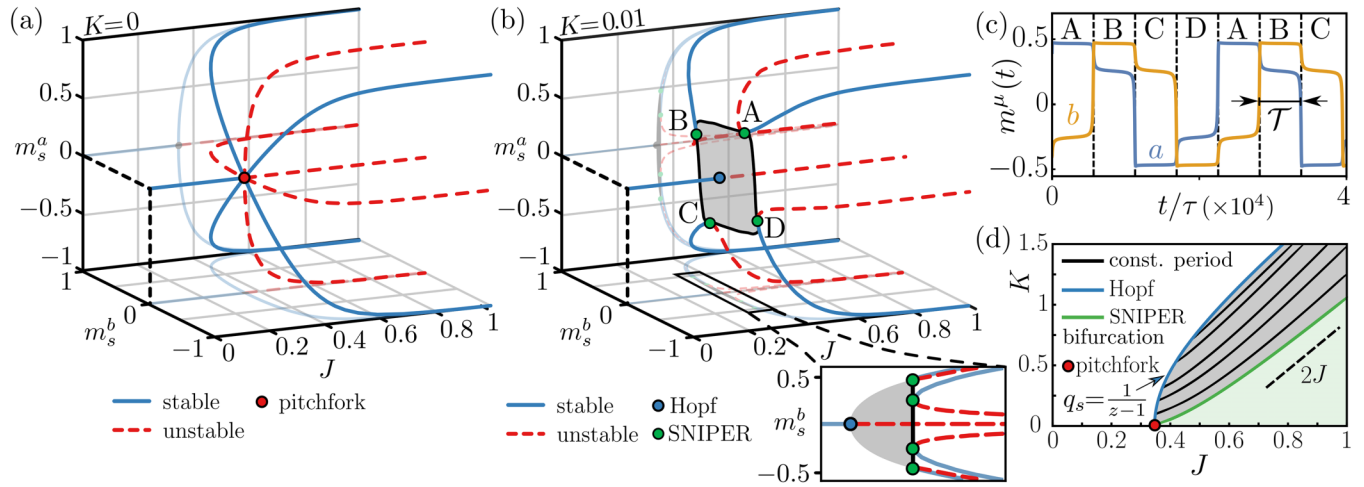

FIG. 2. (a), (b) Bifurcation diagram of the magnetization (m_s^a, m_s^b) in the absence [(a) K=0] and presence [(b) K=0.01] of nonreciprocal coupling as a function of J. Inset of (b): Magnification of the bifurcation diagram around the Hopf bifurcation projected onto the (m_s^b, J) plane (see black box). (c) Temporal evolution of the magnetization for $(J, K) = (0.35991, 0.01)$ close to the degenerate saddle-node-infinite-period (SNIPER) bifurcation at $J_{\mathrm{SNP}}(K)$. The magnetization oscillates coherently between four ghost states A→B→C→D (for K<0 the direction is reversed), which eventually terminate in the four respective stable branches at and beyond the SNIPER bifurcation. The lifetime $\mathcal{T}$ in these ghost states diverges upon approaching $J_{\mathrm{SNP}}(K)$ (see Fig. 3). (d) Phase diagram of m_s^μ: the gray region depicts the regime of coherent oscillations, with the black lines indicating isolines with fixed oscillation period, and the blue line indicating the Hopf bifurcations where $q_s = q_{\mathrm{crit}}$ [Eq. (20)]; in the light-green region the magnetization is stationary and nonzero. In all panels we consider $z = 4$.

branches exhibit nonzero equilibrium magnetization because of spontaneously broken symmetry in both lattices.

Upon setting $K \neq 0$, the pitchfork bifurcation turns into a Hopf bifurcation [blue dot in Fig. 2(b)], whose J value depends on K through the relation $q_s(J, K) = q_{\mathrm{crit}}$ [blue line in Fig. 2(d); see Appendix C for explicit results]. Increasing J beyond the Hopf bifurcation, there is a regime with coherent oscillations [gray area in Figs. 2(b) and 2(d)]. In Fig. 2(d) we identify the isolines of fixed-period oscillations (black lines). Upon further increasing J at fixed K, we observe a nonlinear transition from coherent oscillations to a nonzero steady magnetization [light-green region in Fig. 2(d)], which is set by a degenerate saddle-node-infinite-period (SNIPER) bifurcation [green dots in Fig. 2(b)]. Approaching the SNIPER bifurcation from below, the magnetization in both lattices starts to oscillate between four long-lived ghost states [see Fig. 2(c)]. These four long-lived states correspond to the virtual configuration, in which the respective lattices exert a quasistatic magnetic field on each other, and are characterized by a critical slowing down of the dynamics in the vicinity of the impending SNIPER bifurcation. The residence time within these ghost states diverges algebraically as (see Fig. 3)

$$\mathcal{T} \propto [J_{\mathrm{SNP}}(K) - J]^{-1/2}, \tag{23}$$

where $J_{\mathrm{SNP}}(K)$ is the J value of the SNIPER bifurcation at a given K [green line in Fig. 2(d)]. At the SNIPER bifurcation, four pairs of one stable branch [blue lines in Fig. 2(b)] and one unstable branch [red dashed lines in Fig. 2(b)] emerge. Note that these stable states with nonzero stationary magnetization also exist on the finite square lattice system (see proof in [34]).

The bifurcation diagram obtained with the mean-field approximation has similar qualitative features as in Figs. 2(a) and 2(b) (i.e., a Hopf and SNIPER bifurcation); however, the phase diagram displays a constant Hopf line at a fixed J, independent of K (see [7] and Fig. 5). In Fig. 2(d) we see that the Hopf line with the BG approximation is K-dependent, closely resembling the empirical phase diagram on the cubic lattice (see [7]).

V. SPATIOTEMPORAL DYNAMICS

The results in Figs. 1(d)–1(f) reveal a high degree of local order in the coherent oscillatory regime. To systematically analyze spatiotemporal patterns in states with coherent oscillations, we perform discrete-time Monte Carlo simulations of the nonreciprocal Ising system with $2 \times N \approx 3 \times 10^3$ spins on the all-to-all (z=N), the z=4 Bethe, and the square lattice

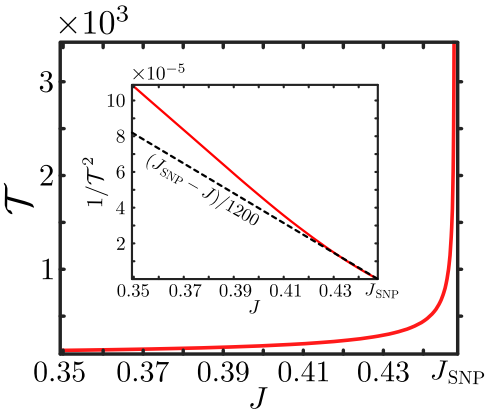

FIG. 3. Algebraic divergence of the residence time $\mathcal{T}$ within a ghost state close to the degenerate saddle-node-infinite-period (SNIPER) bifurcation. Approaching the SNIPER bifurcation from below, the residence time diverges algebraically according to Eq. (23). Here, we have $K = 0.1$ and $z = 4$, for which the SNIPER bifurcation occurs at $J_{\mathrm{SNP}} \approx 0.4477$. Results are obtained with the continuation package MATCONT [37].

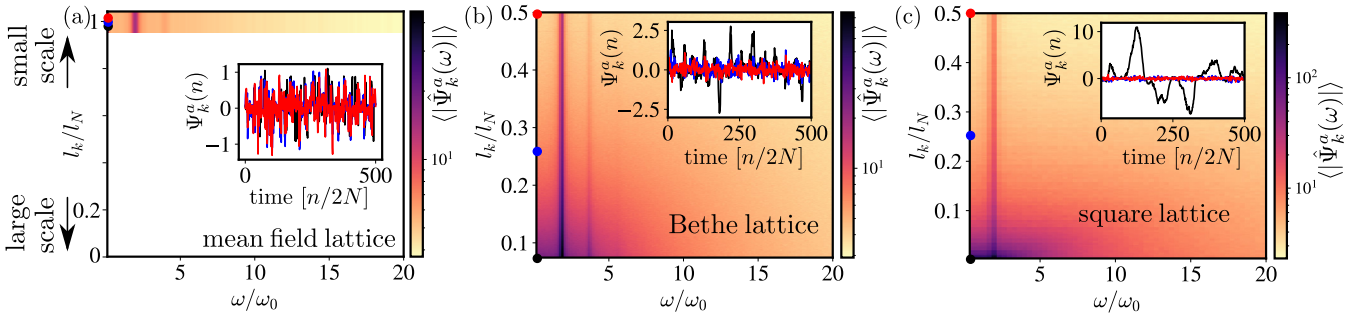

FIG. 4. (a)–(c) Spectral density $\langle|\hat{\Psi}_k^a(\omega)|\rangle$ of modes of coherent oscillations [Eq. (24)] on the (a) mean-field, (b) Bethe, and (c) square lattice (see [34] for animations of the dynamics on the lattices). Note that the nonzero eigenvalues of the mean-field lattice are degenerate, which explains the white region in (a). The values for J are chosen in the respective oscillatory regimes (see Appendix G for details), and $K = 0.3$ for all three lattices. $\langle|\hat{\Psi}_k^a(\omega)|\rangle$ is averaged over 500 independent trajectories, and $\omega_0 = \text{argmax}\langle|\hat{\Psi}_1^a(\omega)|\rangle$ is the natural oscillation frequency. Resonances are visible at multiples of $2\omega_0$, since we ignore the sign of projections. Insets: Temporal development of the projected microscopic states onto the eigenvectors of the Laplacian matrix of respective lattices. Colors denote three selected eigenvalues (and thus spatial scales) indicated by the dots in the main plot.

with periodic boundary conditions. The respective systems are described in detail in Appendix G. For a consistent notion of "spatial scale" on all lattices, we perform a graph-spectral analysis [38].

Let $\mathbf{L}$ be the $N\times N$ symmetric Laplacian matrix of one of the above graphs with elements $L_{ii}=z$, $L_{ij}=-1$ when spins i and j are connected, and $L_{ij}=0$ otherwise. The Laplacian has N orthonormal eigenvectors $\mathbf{L}\boldsymbol{\psi}_k=l_k\boldsymbol{\psi}_k$, $k\in\{1,...,N\}$ with corresponding eigenvalues l_k ordered as $l_1\leqslant\cdots\leqslant l_N$. The lowest eigenvalue, corresponding to $\boldsymbol{\psi}_1=N^{-1/2}(1,\ldots,1)^{\mathrm{T}}$, vanishes, i.e., $l_1=0$ [39]. For the mean-field lattice, all remaining $N-1$ eigenvalues are degenerate, $l_2=\ldots=l_N=N$ [40], but not for the square and Bethe lattices (see Fig. 6).

We express the microscopic state of the lattice μ in time step $n\in\{0,...,n_{\max}\}$ as a column vector $\boldsymbol{\sigma}^\mu(n)=[\sigma_1^\mu(n),...,\sigma_N^\mu(n)]^{\mathrm{T}}$ and project it onto the respective eigenvectors, $\Psi_k^\mu(n)\equiv\boldsymbol{\psi}_k^{\mathrm{T}}\boldsymbol{\sigma}^\mu(n)$. These spatial modes are shown as insets in Figs. 4(a)–4(c), where we see that for the Bethe and square lattice oscillations are pronounced on large scales (small k) and suppressed on small scales (large k). In the mean-field system the spatial modes are equal on all scales due to the degenerate eigenvalues.

To unravel the spatiotemporal structure, we compute the spectral density via the discrete Fourier transform,

$$\left\langle\left|\hat{\Psi}_k^\mu(\omega)\right|\right\rangle\equiv\left\langle\left|\sum_{n=0}^{n_{\max}}\left|\Psi_k^\mu(n)\right|e^{-i2\pi\omega n/n_{\max}}\right|\right\rangle, \tag{24}$$

where $\langle\cdot\rangle$ indicates averaging over independent trajectories and the absolute value takes into account that the sign of the projection is immaterial. The results are shown in Figs. 4(a)–4(c) for coherent oscillations on the a lattice (those for the b lattice are equivalent), with resonances at even multiples of the respective natural frequency $\omega_0=\text{argmax}\langle|\hat{\Psi}_1^a(\omega)|\rangle$, which is the most dominant frequency in the spectrum and scales as $\omega_0\propto 1/\mathcal{T}$ close to the SNIPER bifurcation. The spatiotemporal dynamics on the Bethe and square lattices is qualitatively the same, with small-scale and high-frequency modes suppressed. Thus, coherent oscillations are carried by large-scale low-frequency modes, which agrees with the large local correlations $\mathcal{C}^{\mu\mu}(t)$ shown in Fig. 1(e).

VI. CONCLUDING REMARKS

We have explained the collective dynamics of the nonreciprocal Ising system on the level of both local and global order beyond the mean-field approximation. A critical threshold magnitude of local order within the respective lattices was found to control the emergence of coherent oscillations of the global order parameter. Upon increasing interactions, ghost states emerge and the residence time in either of them eventually diverges, giving rise to a dynamically trapped terminal state via a saddle-node-infinite-period bifurcation. The terminal state depends on the initial condition; the dynamics in this regime is thus nonergodic.

Strikingly, during coherent oscillations of global order, a high degree of local order is preserved [see Fig. 1(d)]. This implies nontrivial spatiotemporal correlations between spins, confirmed by a spectral-density maximum at large-scale low-frequency modes. In stark contrast, on the mean-field (all-to-all) lattice there is no distinction between different spatial modes, annihilating any notion of spatial structure. Thus, accounting for nearest-neighbor correlations is essential for a correct understanding of the dynamics of nonreciprocal matter with a short, or more generally, finite range of interactions.

Our work provides a comprehensive microscopic understanding of dynamic collective phenomena in nonreciprocal matter without conservation laws based on the nonreciprocal Ising model. What remains elusive are multiple (>2) coupled lattices, spatially heterogeneous/extended systems [41], as well as the thermodynamic cost of dynamical states and bifurcations [42–45]. Moreover, considering the relevance of conservation laws [13,16,46,47], it will be essential to develop a theoretical framework for the nonreciprocal Ising model with Kawasaki dynamics. These will be addressed in future work.

ACKNOWLEDGMENTS

Financial support from the German Research Foundation (DFG) through the Heisenberg Program Grants No. GO 2762/4-1 and No. GO 2762/5-1 (to A.G.) is gratefully acknowledged.

APPENDIX A: DERIVATION OF EQS. (8)–(10)

From the master equation (2), we directly obtain dynamical equations for the first two moments of single-spin values [see also Eqs. (28) and (29) in [26]]:

$$\tau \frac{\mathrm{d}\langle \sigma_i^\mu(t)\rangle}{\mathrm{d}t} + \langle \sigma_i^\mu(t)\rangle = \langle \sigma_i^\mu(t)\tanh\left(\Delta E_i^\mu/2\right)\rangle, \tag{A1}$$

$$\tau \frac{\mathrm{d}\langle \sigma_i^\mu(t)\sigma_j^\nu(t)\rangle}{\mathrm{d}t} + 2\langle \sigma_i^\mu(t)\sigma_j^\nu(t)\rangle = \langle \sigma_i^\mu(t)\sigma_j^\nu(t)\left[\tanh\left(\Delta E_i^\mu/2\right) + \tanh\left(\Delta E_j^\nu/2\right)\right]\rangle, \tag{A2}$$

where $\langle f(t)\rangle \equiv \sum_{\boldsymbol{\sigma}} P(\boldsymbol{\sigma};t) f(\boldsymbol{\sigma})$. Equations (A1) and (A2) are exact (but not yet closed) equations for the first two moments evolving under Glauber dynamics, and will serve as our starting point to derive equations for the global and local order parameters, which we derive in two steps: First, we sum Eqs. (A1) and (A2) over all spins and spin pairs. Upon doing this, the left-hand sides of Eqs. (A1) and (A2) transform into

$$\frac{1}{N}\sum_{i=1}^{N}\left(\tau \frac{\mathrm{d}\langle \sigma_i^\mu(t)\rangle}{\mathrm{d}t} + \langle \sigma_i^\mu(t)\rangle\right) = \tau \frac{\mathrm{d}m^\mu(t)}{\mathrm{d}t} + m^\mu(t), \tag{A3}$$

$$\frac{1}{zN}\sum_{i=1}^{N}\sum_{\langle i|j\rangle}\left(\tau \frac{\mathrm{d}\langle \sigma_i^\mu(t)\sigma_j^\mu(t)\rangle}{\mathrm{d}t} + 2\langle \sigma_i^\mu(t)\sigma_j^\mu(t)\rangle\right) = \tau \frac{\mathrm{d}q^{\mu\mu}(t)}{\mathrm{d}t} + 2q^{\mu\mu}(t), \tag{A4}$$

$$\frac{1}{N}\sum_{i=1}^{N}\left(\tau \frac{\mathrm{d}\langle \sigma_i^a(t)\sigma_i^b(t)\rangle}{\mathrm{d}t} + 2\langle \sigma_i^a(t)\sigma_i^b(t)\rangle\right) = \tau \frac{\mathrm{d}q^{ab}(t)}{\mathrm{d}t} + 2q^{ab}(t). \tag{A5}$$

Second, we need to evaluate the right-hand sides of Eqs. (A1) and (A2) after summation over all spins and spin pairs. To do this, we note that ΔE_i^μ can take on a discrete (enumerable) set of values. Consider a spin with $l \in \{0, 1, ..., z\}$ neighboring up spins on the same lattice and $n \in \{0, 1\}$ neighboring up spins on the opposing lattice. We want to compute the change in energy upon flipping this spin. Based on Eq. (1) we can parametrize this change in energy upon flipping the spin as

$$\Delta E_i^\mu = 2\sigma_i^\mu U_{l,n}^\mu, \tag{A6}$$

where $U_{l,n}^\mu$ is given by Eq. (11). Using this parametrization, we evaluate the right-hand sides of Eqs. (A1) and (A2)

$$\frac{1}{N}\sum_{i=1}^{N}\langle \sigma_i^\mu \tanh\left(\Delta E_i^\mu/2\right)\rangle = \frac{1}{N}\sum_{i=1}^{N}\langle \tanh\left(U_{l,n}^\mu\right)\rangle = \sum_{l=0}^{z}\sum_{n=0}^{1}\mathcal{P}_{l,n}^\mu(t)\tanh\left(U_{l,n}^\mu\right), \tag{A7}$$

$$\frac{1}{zN}\sum_{i=1}^{N}\sum_{\langle i|j\rangle}\langle \sigma_i^\mu\sigma_j^\mu \tanh\left(\Delta E_i^\mu/2\right)\rangle = \frac{1}{zN}\sum_{i=1}^{N}\sum_{\langle i|j\rangle}\langle \sigma_j^\mu \tanh\left(U_{l,n}^\mu\right)\rangle = \frac{1}{z}\sum_{l=0}^{z}\sum_{n=0}^{1}(2l-z)\mathcal{P}_{l,n}^\mu(t)\tanh\left(U_{l,n}^\mu\right), \tag{A8}$$

$$\frac{1}{N}\sum_{i=1}^{N}\langle \sigma_i^a\sigma_i^b \tanh\left(\Delta E_i^a/2\right)\rangle = \frac{1}{N}\sum_{i=1}^{N}\langle \sigma_i^b \tanh\left(U_{l,n}^a\right)\rangle = \sum_{l=0}^{z}\sum_{n=0}^{1}(2n-1)\mathcal{P}_{l,n}^\mu(t)\tanh\left(U_{l,n}^a\right). \tag{A9}$$

For the first equality in Eqs. (A7)–(A9) we used $\tanh\left(\Delta E_i^\mu/2\right) = \tanh\left(\sigma_i^\mu U_{l,n}^\mu\right) = \sigma_i^\mu \tanh\left(U_{l,n}^\mu\right)$, together with $(\sigma_i^\mu)^2 = 1$. For the second equality, we note that terms such as $\langle \tanh\left(U_{l,n}^\mu\right)\rangle$ represent a weighted sum over all possible combinations of the possible values that $\tanh\left(U_{l,n}^\mu\right)$ can attain. The weights are given by the time-dependent probability $\mathcal{P}_{l,n}^\mu(t)$ to find an up or down spin with a specific local environment. By definition, this probability is normalized $\sum_{l,n}\mathcal{P}_{l,n}^\mu(t) = 1$. Combining Eqs. (A3)–(A5) and (A7)–(A9) we obtain Eqs. (8)–(10).

APPENDIX B: DERIVATION OF EQ. (14)

Here, we derive Eq. (14) based on the BG approximation. We focus on the probability of picking a spin on the a lattice with a given specific local environment. The same reasoning will also apply for picking a spin on the b lattice. Recall that $\mathcal{P}_{l,n}^{a\pm}(t)$ is the probability at time t to find an up (+) or down (–) spin with l neighboring up spins on the a lattice and n neighboring up spins on the b lattice. On the BG level, we assume ideal mixing of nearest-neighbor spin pairs,

resulting in the following expressions:

$$\mathcal{P}_{l,n}^{a+} = \underbrace{[N_+^a/N]}_{\substack{\text{probability}\\ \text{for up spin}\\ \text{on the } a \text{ lattice}}} \times \underbrace{\left[\binom{N_{++}^{aa}}{l}\binom{N_{+-}^{aa}/2}{z-l}\Big/\binom{N_{++}^{aa}+N_{+-}^{aa}/2}{z}\right]}_{\substack{\text{probability for}\\ l \text{ neighboring up}\\ \text{spins on the } a \text{ lattice}}} \times \underbrace{\left[\binom{N_{++}^{ab}}{n}\binom{N_{+-}^{ab}}{1-n}\Big/\binom{N_{++}^{ab}+N_{+-}^{ab}}{1}\right]}_{\substack{\text{probability for}\\ n \text{ neighboring up}\\ \text{spins on the } b \text{ lattice}}}, \tag{B1}$$

$$\mathcal{P}_{l,n}^{a-} = \underbrace{[N_-^a/N]}_{\substack{\text{probability}\\ \text{for down spin}\\ \text{on the } a \text{ lattice}}} \times \underbrace{\left[\binom{N_{-+}^{aa}/2}{l}\binom{N_{--}^{aa}}{z-l}\Big/\binom{N_{-+}^{aa}/2+N_{--}^{aa}}{z}\right]}_{\substack{\text{probability for}\\ l \text{ neighboring up}\\ \text{spins on the } a \text{ lattice}}} \times \underbrace{\left[\binom{N_{-+}^{ab}}{n}\binom{N_{--}^{ab}}{1-n}\Big/\binom{N_{-+}^{ab}+N_{--}^{ab}}{1}\right]}_{\substack{\text{probability for}\\ n \text{ neighboring up}\\ \text{spins on the } b \text{ lattice}}}, \tag{B2}$$

where, for example, N_{+-}^{ab} is the total number of nearest-neighbor spin pairs with an up spin on the a lattice and a down spin on the b lattice. To relate N_{+-}^{ab} and the other spin pair numbers to the global and local order, we make use of the following exact relations for periodic lattices:

$$2N_{\pm\pm}^{\mu\mu} + N_{+-}^{\mu\mu} = zN_{\pm}^{\mu}, \tag{B3}$$

$$N_{\pm\pm}^{ab} + N_{\pm\mp}^{ab} = N_{\pm}^{a}, \tag{B4}$$

in combination with

$$N_{\pm}^{\mu} = N(1 \pm m^{\mu})/2. \tag{B5}$$

Furthermore, we use the definition of local order given by Eqs. (5) and (6) to write

$$\begin{aligned} q^{\mu\mu} &= 2(N_{++}^{\mu\mu} + N_{--}^{\mu\mu} - N_{+-}^{\mu\mu})/zN \\ &= 1 - 4N_{+-}^{\mu\mu}/zN, \end{aligned} \tag{B6}$$

$$\begin{aligned} q^{ab} &= (N_{++}^{ab} + N_{--}^{ab} - N_{+-}^{ab} - N_{-+}^{ab})/N \\ &= 1 - 2N_{+-}^{ab}/N - 2N_{-+}^{ab}/N \\ &= 1 + m^a - m^b - 4N_{+-}^{ab}/N, \end{aligned} \tag{B7}$$

where in the last line we used the relation

$$m^b - m^a = 2(N_{-+}^{ab} - N_{+-}^{ab})/N. \tag{B8}$$

Using the relations (B3)–(B7) we obtain the following expression for the spin pairs within the same lattice:

$$N_{\pm\pm}^{\mu\mu} = (z/8)N(1 \pm 2m^{\mu} + q^{\mu\mu}), \tag{B9}$$

$$N_{\pm\mp}^{\mu\mu} = (z/4)N(1 - q^{\mu\mu}), \tag{B10}$$

and for the spin pairs between the two opposing lattices

$$N_{\pm\pm}^{ab} = (1/4)N(1 \pm m^a \pm m^b + q^{ab}), \tag{B11}$$

$$N_{\pm\mp}^{ab} = (1/4)N(1 \pm m^a \mp m^b - q^{ab}). \tag{B12}$$

Inserting Eqs. (B9)–(B12) into Eqs. (B1) and (B2) and taking the thermodynamic limit $N \to \infty$ while keeping $m^{\mu}(t)$, $q^{\mu\mu}(t)$, and $q^{ab}(t)$ fixed, we obtain Eq. (14).

APPENDIX C: STEADY-STATE LOCAL ORDER

The trivial steady state is given by the disordered state with $m_s^{\mu} = 0$ and $q_s^{ab} = 0$. To solve for the steady state of the local order, denoted as $q_s(J, K)$, we need to solve

$$q_s(J,K) = \frac{1}{z}\sum_{l=0}^{z}\sum_{n=0}^{1}(2l - z)(\overline{\mathcal{P}}_l^{+} + \overline{\mathcal{P}}_l^{-})\tanh\left(U_{l,n}^{a}\right), \tag{C1}$$

where $\overline{\mathcal{P}}_l^{\pm}(q_s)$ are the probabilities (14) evaluated at steady-state values given by Eq. (19). Equation (C1) can be solved for specific integer values of z. For example, for $z = 2$ we obtain

$$q_s(J,K)|_{z=2} = \frac{2 - \sqrt{4 - \left[\sum_{n=\pm}\tanh(2J + nK)\right]^2}}{\sum_{n=\pm}\tanh(2J + nK)}.$$

For $z = 4$, the solution can be written as

$$q_s(J,K)|_{z=4} = \mathcal{S}(J,K) - (1/2)\sqrt{-4\mathcal{S}(J,K)^2 + 2\mathcal{H}(J,K) + \mathcal{Q}(J,K)/\mathcal{S}(J,K)}, \tag{C2}$$

where we have introduced the auxiliary functions

$$\mathcal{H}(J,K) \equiv \frac{3\cosh(4J)[\cosh(4J) + \cosh(2K)]}{\sinh^2(2J)[\cosh(4J) - 2\sinh^2(K)]}, \tag{C3}$$

$$\mathcal{Q}(J,K) \equiv 16\left(\sum_{n=\pm}[\tanh(4J + nK) - 2\tanh(2J + nK)]\right)^{-1}, \tag{C4}$$

$$\mathcal{S}(J,K) \equiv (1/2)\sqrt{(2/3)\mathcal{H}(J,K) + [\mathcal{Q}(J,K)/6][\mathcal{A}(J,K) + \Delta_0(J,K)/\mathcal{A}(J,K)]}, \tag{C5}$$

$$\mathcal{A}(J,K) \equiv 2^{-1/3}\left(\Delta_1(J,K) + \sqrt{\Delta_1^2(J,K) - 4\Delta_0^3(J,K)}\right)^{1/3}, \tag{C6}$$

$$\Delta_0(J,K) \equiv -(3/4)\sum_{n=\pm}[\tanh(2J+nK)+\tanh(4J+nK)]\sum_{n=\pm}[\tanh(2J+nK)-\tanh(4J+nK)], \tag{C7}$$

$$\Delta_1(J,K) \equiv 216\cosh(2J)\cosh(2K)\mathrm{sech}(4J-K)\mathrm{sech}(4J+K)\sinh^3(2J)\sinh^2(K)[\cosh(4J)+\cosh(2K)]^{-2}. \tag{C8}$$

APPENDIX D: OSCILLATORY INSTABILITY

Here, we prove that $M_2(q_s;J,K\neq 0)\neq 0$. To see this, we explicitly write out the first sum over n in Eq. (18):

$$M_2(q_s;J,K) = \sum_{l=0}^{z}(\overline{\mathcal{P}}_l^{+}+\overline{\mathcal{P}}_l^{-})[\tanh([2l-z]J+K) - \tanh([2l-z]J-K)]. \tag{D1}$$

Note that $\overline{\mathcal{P}}_l^{\pm}(q_s)>0$ for $q_s\in(-1,1)$, which follows straightforwardly from Eq. (19). Furthermore, since $\tanh(x)$ is an increasing function of x, we have $\tanh([2l-z]J+K)-\tanh([2l-z]J-K)>0$ for $K>0$ and $\tanh([2l-z]J+K)-\tanh([2l-z]J-K)<0$ for $K<0$. Hence, $M_2(q_s;J,K)$ is given by a sum over strictly positive (for $K>0$) or negative (for $K<0$) terms, rendering $M_2(q_s;J,K\neq 0)\neq 0$. This results in complex eigenvalues for $\lambda_{\pm}(q_s;J,K)$ as shown in Fig. 1(b).

APPENDIX E: MEAN-FIELD APPROXIMATION

A less accurate technique to obtain approximate evolution equations is the mean-field (MF) approximation (originally developed in [48]), where one makes the rudimentary (uncontrolled) assumption

$$\left\langle\tanh\left(\Delta E_i^{\mu}/2\right)\right\rangle \approx \tanh\left\langle\Delta E_i^{\mu}/2\right\rangle, \tag{E1}$$

yielding the evolution equations

$$\begin{aligned}\tau\frac{\mathrm{d}m^a(t)}{\mathrm{d}t}+m^a(t)&=\tanh[zJ_am^a(t)+K_am^b(t)],\\ \tau\frac{\mathrm{d}m^b(t)}{\mathrm{d}t}+m^b(t)&=\tanh[zJ_bm^b(t)+K_bm^a(t)],\end{aligned} \tag{E2}$$

which are exact on the fully connected mean-field lattice, where the local order is trivial (i.e., there is no sense of "local"), $q^{\mu\nu}(t)=m^{\mu}(t)m^{\nu}(t)$, and therefore $\mathcal{C}^{\mu\nu}(t)=0$. A linear stability analysis around the trivial steady state $m_s^{\mu}=0$ for $J_a=J_b=J$ and $K_a=-K_b=K$ leads to a linear stability equation where the eigenvalues of the linear stability matrix are given by

$$\lambda_{\pm}^{\mathrm{MF}}(J,K) = (zJ-1)\pm iK. \tag{E3}$$

Hence, the Hopf bifurcation occurs at $J=1/z$ and $K\neq 0$, such that $\mathrm{Re}(\lambda_{\pm}^{\mathrm{MF}})=0$ and $\mathrm{Im}(\lambda_{\pm}^{\mathrm{MF}})\neq 0$. This corresponds to a straight vertical line in the (J,K) plane, as shown in Fig. 5(a) and also found in [7]. Notably, in the MF approximation we do not observe a critical value for local order, which is present in the more accurate BG approximation.

APPENDIX F: MONOMER APPROXIMATION

Another approximation technique we developed in this work is what we call the "monomer approximation." It is more accurate than the MF but less accurate than the BG approximation.

The conceptual difference between the MF on the one hand, and the monomer and BG approximations on the other hand, lies in the treatment of the average $\langle\tanh(\Delta E_i^{\mu}/2)\rangle$. Whereas the MF approximation simply moves the average to the argument as shown in Eq. (E1), the monomer and BG approximations use the fact that the value of $\Delta E_i^{\mu}/2$ lies in an enumerable set given by $U_{l,n}^{\mu}\equiv[2l-z]J_{\mu}+[2n-1]K_{\mu}$ with $l\in\{0,..,z\}$ and $n\in\{0,1\}$. This allows for an explicit summation

$$\left\langle\tanh\left(\Delta E_i^{\mu}/2\right)\right\rangle = \sum_{l=0}^{z}\sum_{n=0}^{1}\mathcal{P}_{l,n}^{\mu}(t)\tanh\left(U_{l,n}^{\mu}\right), \tag{F1}$$

where only the probability $\mathcal{P}_{l,n}^{\mu}(t)$ has to be approximated.

Similar to the BG approximation, the resulting evolution equations in the monomer approximation are governed by Eqs. (8)–(10), but the time-dependent probabilities are different and read (the derivation is given in [34])

$$\mathcal{P}_{l,n}^{a}(t) = \frac{2\mathcal{C}_l^z[1+m^a(t)]^l[1+m^b(t)]^n}{[1-m^a(t)]^{l-z}[1-m^b(t)]^{n-1}}, \tag{F2}$$

and $\mathcal{P}_{l,n}^{b}(t)$ is obtained by replacing $m^a(t)$ with $m^b(t)$ in Eq. (F2). Since $\mathcal{P}_{l,n}^{a}(t)$ is independent of the local order $q^{\mu\nu}(t)$, this implies that $q^{\mu\nu}(t)$ is slaved by $m^{\mu}(t)$; however, $q^{\mu\nu}(t)\neq m^{\mu}(t)m^{\nu}(t)$. Performing a linear stability analysis around the trivial steady state $m_s^{\mu}=0$ for $J_a=J_b=J$ and $K_a=-K_b=K$, we obtain a linear stability equation where the eigenvalues of the linear stability matrix can neatly be written as

$$\hat{\lambda}_{\pm}(q_s;J,K) = [zq_s(J,K)-1]\pm i\hat{M}_2(J,K), \tag{F3}$$

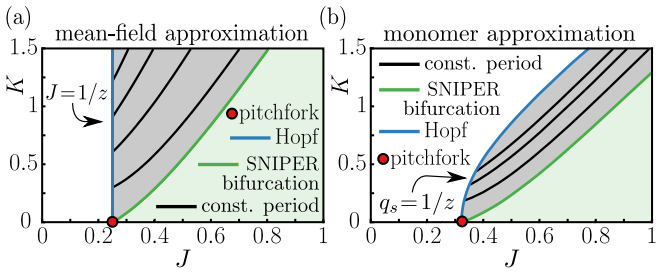

FIG. 5. Phase diagram for global order m_s^{μ} obtained with the mean-field (MF) approximation (a) and the monomer approximation (b) for the perfect nonreciprocal setting with $J_a=J_b=J$ and $K_a=-K_b=K$. In the MF approximation the Hopf bifurcation (blue line) is set by $J=1/z$. In the monomer approximation, the Hopf bifurcations (blue line) are set by a critical local order $q_s=1/z$, which is more similar to the Bethe-Guggenheim approximation where $q_s=1/(z-1)$ [see Fig. 2(d)].

TABLE I. Overview of approximation techniques and their dynamical equations.

Approx. technique	$m^{\mu}(t)$	$q^{\mu\nu}(t)$	Hopf
MF	(E2)	$= m^{\mu}(t)m^{\nu}(t)$	$J{=}1/z$
Monomer	(8)+(F2)	(9)–(10)+(F2); slaved by $m^{\mu}(t)$	$q_s{=}1/z$
BG	(8)+(14)	(9)–(10)+(14); not slaved	$q_s{=}1/(z{-}1)$

where $q_s(J,K)$ is the steady-state value of the local order in the monomer approximation, and

$$\hat{M}_2(J,K) = 2\sum_{l=0}^{z}\sum_{n=0}^{1}(2n-1)\mathcal{C}_l^z \tanh\left(U_{l,n}^a\right). \tag{F4}$$

From this follows that the Hopf bifurcation occurs at $q_s = 1/z$ and $K \neq 0$, such that $\mathrm{Re}(\hat{\lambda}_{\pm}) = 0$ and $\mathrm{Im}(\hat{\lambda}_{\pm}) \neq 0$. Hence, as within the BG approximation, we also find the existence of a critical local order in the monomer approximation. Contrary to the MF approximation, the Hopf line is not a straight vertical line in the (J,K) plane, as shown in Fig. 5(b).

To provide a concise overview of the various approximation techniques, we summarize in Table I the respective evolution and conditions for the Hopf bifurcation.

APPENDIX G: KINETIC MONTE CARLO SIMULATIONS

For the results shown in Figs. 1(c), 1(d) (black dashed lines), and 4 we performed kinetic Monte Carlo (MC) simulations on three different types of lattices: (i) the fully connected MF lattice, (ii) the Bethe lattice, and (iii) the square lattice with periodic boundary conditions. Simulations on the Bethe lattice were performed using the random graph algorithm [31,32], which works as follows: Consider a Bethe lattice with coordination number z. First, we create a Cayley tree of $i = \{1, ..., N\}$ spins with coordination number z. The spins on the outer layer are connected to one spin on the inner layer. To create the remaining $z-1$ connections, we randomly pair spins on the outer layer to other spins on the outer layer. The final result is a Cayley tree with random connections on the outer layer. Note that for both lattices a and b we create new random connections. For large N, it has been shown that the Ising model on an ensemble of such random graphs is equivalent to the Ising model on a Bethe lattice [31]. Indeed, for large N we find perfect agreement between the simulations and our theory, as shown in Figs. 1(c) and 1(d). For the MF lattice, we connect all spins with each other, resulting in a fully connected graph.

TABLE II. Simulation parameters for results shown in Fig. 4.

Lattice	size (N)	MC steps	No. traj.	J (k_BT)	K (k_BT)
Mean field	1500	$N \times 10^3$	500	$1.5/N$	0.3
Bethe	1457	$N \times 10^3$	500	0.5	0.3
square	40×40	$N \times 10^3$	500	0.6	0.3

1. Simulation setup

In Table II we summarize the size of the system, the number of trajectories, and the parameter settings that were used to obtain the spectral density shown in Fig. 4. As initial conditions, we selected a randomly mixed configuration of up and down spins for fixed magnetization.

For the results shown in Figs. 1(c) and 1(d) we used a Bethe lattice with system size $N = 118\,097$. Such a large system size was not feasible for the setup of Fig. 4 since the spectral density $\langle|\hat{\Psi}_k^{\mu}(\omega)|\rangle$ must be averaged over many independent trajectories, resulting in memory issues for too large N.

2. Eigenvalues of Laplacian matrix

In Fig. 4 we plot the spectral density $\langle|\hat{\Psi}_k^{\mu}(\omega)|\rangle$ as a function of the eigenvalues l_k of the Laplacian matrix $\mathbf{L}$. To obtain the eigenvalues, we numerically diagonalized the Laplacian $\mathbf{L}$ in Python, and the resulting eigenvalues are shown in Fig. 6. Note that for the mean-field lattices, all eigenvalues except the first are degenerate and equal to $l_2 = \cdots = l_N = N$.

3. Animations

To visualize the dynamics of the nonreciprocal Ising model on the mean-field lattice, Bethe lattice, and square lattice, we have provided animations in [34]. In each animation, we show three independent simulations on the aforementioned lattices, with the coupling strengths (J,K) reported in Table II. More information about the animations is given below:

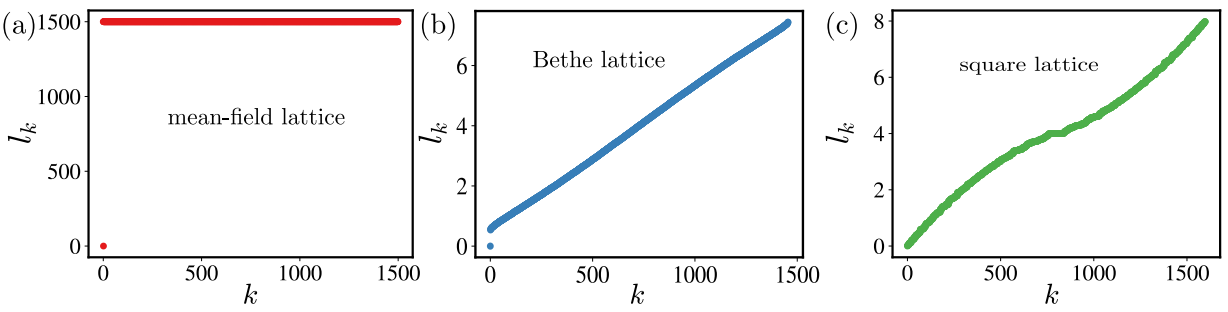

FIG. 6. Eigenvalues l_k of the Laplacian matrix $\mathbf{L}$ for the mean-field lattice (a), Bethe lattice (b), and square lattice (c). For the mean-field lattice, all eigenvalues except for the first are degenerate with value $l_2 = ... = l_N = N$, where N is the system size given in Table II. The Bethe lattice has a spectral gap between the lowest eigenvalue $l_1 = 0$ and l_2.

(1) "MF_lattice.gif" shows simulations on the mean-field lattice for $N = 2000$ spins, where each spin is connected to every other spin. For illustrative purposes, the edges between spins are not shown.

(2) "Bethe_lattice.gif" shows simulations on the Bethe lattice for $N = 131\,21$ spins, corresponding to a Bethe lattice with eight layers and a coordination number of $z = 4$. For illustrative purposes, only the first six layers of the Bethe lattice are shown.

(3) "Square_lattice.gif" shows simulations on the square lattice for $N = 122 \times 122$ spins.

[1] L. Guislain and E. Bertin, J. Stat. Mech. (2024) 093210.
[2] L. Guislain and E. Bertin, J. Phys. A: Math. Theor. **57**, 375001 (2024).
[3] D. S. Seara, A. Piya, and A. P. Tabatabai, J. Stat. Mech. (2023) 043209.
[4] F. Collet, M. Formentin, and D. Tovazzi, Phys. Rev. E **94**, 042139 (2016).
[5] F. Collet, J. Stat. Phys. **157**, 1301 (2014).
[6] F. Collet and M. Formentin, J. Stat. Phys. **176**, 478 (2019).
[7] Y. Avni, M. Fruchart, D. Martin, D. Seara, and V. Vitelli, The non-reciprocal Ising model, arXiv:2311.05471
[8] S. A. M. Loos, S. H. L. Klapp, and T. Martynec, Phys. Rev. Lett. **130**, 198301 (2023).
[9] L. Guislain and E. Bertin, Phys. Rev. E **109**, 034131 (2024).
[10] S. Osat and R. Golestanian, Nat. Nanotechnol. **18**, 79 (2023).
[11] S. Osat, J. Metson, M. Kardar, and R. Golestanian, Phys. Rev. Lett. **133**, 028301 (2024).
[12] A. V. Ivlev, J. Bartnick, M. Heinen, C.-R. Du, V. Nosenko, and H. Löwen, Phys. Rev. X **5**, 011035 (2015).
[13] F. Brauns and M. C. Marchetti, Phys. Rev. X **14**, 021014 (2024).
[14] M. te Vrugt, M. P. Holl, A. Koch, R. Wittkowski, and U. Thiele, Model. Simul. Mater. Sci. Eng. **30**, 084001 (2022).
[15] T. Frohoff-Hülsmann, J. Wrembel, and U. Thiele, Phys. Rev. E **103**, 042602 (2021).
[16] S. Saha, J. Agudo-Canalejo, and R. Golestanian, Phys. Rev. X **10**, 041009 (2020).
[17] K. John and M. Bär, Phys. Rev. Lett. **95**, 198101 (2005).
[18] T. Frohoff-Hülsmann and U. Thiele, IMA J. Appl. Math. **86**, 924 (2021).
[19] T. Frohoff-Hülsmann, M. P. Holl, E. Knobloch, S. V. Gurevich, and U. Thiele, Phys. Rev. E **107**, 064210 (2023).
[20] R. Mandal, S. S. Jaramillo, and P. Sollich, Phys. Rev. E **109**, L062602 (2024).
[21] T. Frohoff-Hülsmann, U. Thiele, and L. M. Pismen, Philos. Trans. R. Soc. A **381**, 20220087 (2023).
[22] D. Greve, G. Lovato, T. Frohoff-Hülsmann, and U. Thiele, Phys. Rev. Lett. **134**, 018303 (2025).
[23] P. C. Hohenberg and B. I. Halperin, Rev. Mod. Phys. **49**, 435 (1977).
[24] M. Liu, Z. Hou, H. Kitahata, L. He, and S. Komura, J. Phys. Soc. Jpn. **92**, 093001 (2023).
[25] The local interaction energy is not equal to the total energy of the system, since the interaction energy for the two lattices *a* and *b* is different.
[26] R. J. Glauber, J. Math. Phys. **4**, 294 (1963).
[27] Y. Saito and R. Kubo, J. Stat. Phys. **15**, 233 (1976).
[28] L. Guislain and E. Bertin, Phys. Rev. B **109**, 184203 (2024).
[29] L. Guislain and E. Bertin, Phys. Rev. Lett. **130**, 207102 (2023).
[30] K. Blom, *Pair-Correlation Effects in Many-Body Systems: Towards a Complete Theoretical Description of Pair-Correlations in the Static and Kinetic Description of Many-Body Systems* (Springer Nature, Cham, Switzerland, 2023).
[31] D. A. Johnston and P. Plechác, J. Phys. A: Math. Gen. **31**, 475 (1998).
[32] D. Dhar, P. Shukla, and J. P. Sethna, J. Phys. A: Math. Gen. **30**, 5259 (1997).
[33] R. Hanai, Phys. Rev. X **14**, 011029 (2024).
[34] See Supplemental Material at http://link.aps.org/supplemental/10.1103/PhysRevE.111.024207 for further detailed calculations and a note about static order in the nonreciprocal Ising model on the square lattice.
[35] S. H. Strogatz, *Nonlinear Dynamics and Chaos: With Applications to Physics, Biology, Chemistry, and Engineering* (CRC, Boca Raton, FL, 2018).
[36] M. C. Cross and P. C. Hohenberg, Rev. Mod. Phys. **65**, 851 (1993).
[37] A. Dhooge, W. Govaerts, and Y. A. Kuznetsov, ACM Trans. Math. Softw. **29**, 141 (2003).
[38] J. van der Kolk, G. García-Pérez, N. E. Kouvaris, M. A. Serrano, and M. Boguñá, Phys. Rev. X **13**, 021038 (2023).
[39] W. N. Anderson, Jr. and T. D. Morley, Linear Multilinear Algebra **18**, 141 (1985).
[40] R. Cohen and S. Havlin, *Complex Networks: Structure, Robustness and Function* (Cambridge University Press, Cambridge, 2010).
[41] K. Blom, N. Ziethen, D. Zwicker, and A. Godec, Phys. Rev. Res. **5**, 013135 (2023).
[42] T. Suchanek, K. Kroy, and S. A. M. Loos, Phys. Rev. Lett. **131**, 258302 (2023).
[43] C. Nardini, E. Fodor, E. Tjhung, F. van Wijland, J. Tailleur, and M. E. Cates, Phys. Rev. X **7**, 021007 (2017).
[44] K. Blom, K. Song, E. Vouga, A. Godec, and D. E. Makarov, Proc. Natl. Acad. Sci. USA **121**, e2318333121 (2024).
[45] Z. Zhang and R. Garcia-Millan, Phys. Rev. Res. **5**, L022033 (2023).
[46] T. Frohoff-Hülsmann and U. Thiele, Phys. Rev. Lett. **131**, 107201 (2023).
[47] D. Greve and U. Thiele, Chaos **34**, 123134 (2024).
[48] O. Penrose, J. Stat. Phys. **63**, 975 (1991).